Available online at www.sciencedirect.com

ScienceDirect

Advances in Space Research xxx (xxxx) xxx

ADVANCES IN SPACE RESEARCH (a COSPAR publication)

www.elsevier.com/locate/asr

Tetrahedral satellite formation: Geomagnetic measurements exchange and interpolation

Anton Afanasev *, Mikhail Shavin, Anton Ivanov, Dmitry Pritykin

Space Center, Skolkovo Institute of Science and Technology, Russian Federation

Received 2 September 2020; received in revised form 2 February 2021; accepted 8 February 2021

Abstract

This note presents a study of a four-satellite tetrahedral formation to collect, process, and exchange multipoint measurements of geomagnetic field in a near-polar orbit. The study is conducted as a series of numerical experiments based on simulated spacecraft orbits and corresponding geomagnetic field models output. The four satellites are assumed to move in near-circular orbits specifically chosen to maintain the tetrahedron quality. The satellites exchange their simulated magnetometers readings and the collected multipoint measurements are processed on board of any of them thus creating an instantaneous interpolated map of the geomagnetic field in the interior of the tetrahedron. Interpolation is carried out with the use of Kriging algorithms, known in geostatistics for capturing spatial correlation of the data and taking into account statistical properties of the interpolated variables. We propose a concept of a servicing formation, and analyze interpolation accuracy for different formation sizes. It is then discussed how the processed multipoint measurements can be provided as a service to other nearby satellites. Finally, we show that using the existing COTS magnetometers it is possible to obtain real-time interpolation data, which are more precise at a given point and time than a conventional onboard magnetic field model, thus ensuring better attitude determination routines performance in the serviced spacecraft.

Keywords: Formation flying; Multipoint measurements; Geomagnetic field; Interpolation; Attitude determination

1. Introduction

The use of distributed space systems, comprising multiple spacecraft that interact, cooperate and communicate with each other in orbit is an enabler of a large variety of space applications such as synthetic aperture radars (SAR) and optical interferometry, on-orbit inspection and servicing of other spacecraft, spatial gradients measurements of environmental data. Some of these applications, such as distributed SAR (Grasso et al., 2020), are still discussed theoretically, others, such as the Afternoon Train constellation (Stephens et al., 2002) to monitor the Earth's atmosphere and provide 3D reconstructions of climate and weather patterns, have a long success story. Formation flying missions, such as TanDEM-X (Krieger et al., 2007) and PRISMA (Loizzo et al., 2018) proved successful in autonomous relative navigation and control. CanX-4&5 mission (Bonin et al., 2015) demonstrated a projected circular orbit (PCO) formation and maintenance for two satellites of 50 m semi-major axis of the PCO ellipse with sub-meter accuracy. The Swarm-mission (Friis-Christensen et al., 2006) provided multipoint measurements of the geomagnetic field and its temporal evolution that helped to improve our understanding of the Earth's interior and its effect on Geospace.

Satellite formations are often discussed in connection with multipoint electromagnetic or ionospheric plasma

* Corresponding author at: 121205, Bolshoy Boulevard 30, bld. 1, Moscow, Russian Federation.
E-mail address: Anton.Afanasev@skoltech.ru (A. Afanasev).

https://doi.org/10.1016/j.asr.2021.02.012
0273-1177/

measurements (Roscoe et al., 2011; Fish et al., 2014; Nicholas et al., 2019), where it is required to distinguish between temporal and spatial variations of the measured quantity. This latter requirement calls for use of a three-dimensional formation of satellites, the simplest of which is tetrahedral formation such as brought up in Sadeghi and Emami (2017). Speaking of specific needs of ionospheric studies, it is speculated in Chernyshov et al. (2016) that there is a demand for simultaneous measurements of the ionospheric plasma parameters at different spatial scales with a high temporal resolution. The authors propose a tentative orbital configuration for a group of spacecraft, in which a number of satellites follow one another in the same orbit (a train formation), being separated by distances determined by free paths of various ions, with two groups of satellites separated by a distance significantly exceeding 500 m. In order to be able to conduct simultaneous measurements at different distances and in different directions from a reference point moving along the train orbit, the train formation is complemented by two more satellites with slightly different orbital planes to make the formation three-dimensional. It is also discussed that using radiophysical methods (Chernyshov et al., 2020) to measure ionospheric plasma density requires intersatellite distances greater than 1 km.

With this in mind, we start our study by considering a three-dimensional formation, whose structure is similar to the one proposed in Chernyshov et al. (2016), but clusters of closely located satellites are substituted by single points of measurement, thus making the formation a group of four satellites. Two of the satellites are to orbit the Earth in the leader–follower configuration in a near-circular near-polar orbit while the other two must keep the three-dimensional formation nondegenerate. It was stated during the design of the famous Magnetospheric Multiscale mission (Guzman and Edery, 2004) that the best quality of the measurements is achieved by maintaining the shape of the tetrahedron as close to regular as possible. The requirements to the tetrahedron quality can be formalized as a scalar quality parameter (Daly, 1994; Paschmann and Daly, 1998), which is taken into account during the orbit design phase. Following many researchers (e.g. Vaddi et al., 2005; Shestakov et al., 2019), we choose the reference orbits for the formations satellites that ensure the quality of the proposed tetrahedron, which is to be maintained with relatively low fuel consumption.

Having established the orbital motion of the formation spacecraft we proceed with the interpolation of the simulated geomagnetic field multipoint measurements in the interior points of the tetrahedron composed of the four satellites. The main contribution of this study is an example of the multipoint measurements real-time processing and usage. We exemplify it by the four satellites onboard magnetometer data exchange to construct a local geomagnetic field map, which can be provided as a service to any other nearby satellite. To this end we employ the Kriging interpolation technique (Wackernagel, 1995), which originated in geostatistical analysis, and to the best of our knowledge has not been extensively used in space applications. One of its indisputable advantages over other interpolators is the ability to capture a certain degree of continuity inherent in the spatially distributed properties to be measured. This algorithm relies on auto-correlation and variance information about the environment of the magnetic field, which is of utmost importance for nonhomogeneous and noisy fields. We consider various implementations of the interpolator with the use of different semivariogram models constructed for the geomagnetic field on the base of IGRF-13 model by sampling in regions, comparable with the size of the formation.

We propose a four-spacecraft tetrahedral formation that is not only used to collect the data measured by the onboard instruments, but also to processes such data and provide a real-time service to any other satellite in the neighbourhood of such formation. One could envision that such service could be provided even to a larger swarm mission, whose satellites are distributed over the interior of the servicing formation. As an example of such service the interpolation of geomagnetic field in the interior points of the four-satellite tetrahedral formation is considered. The serviced data can be employed in the attitude determination (and control) loop instead of the onboard geomagnetic field model. Our preliminary studies (Mahfouz et al., 2019; Afanasev et al., 2020) have shown that such coordinated data exchange across a group of satellites under certain assumptions leads to the overall enhancement of magnetometer-based attitude determination routines in each individual spacecraft in the group. The data-exchanging swarm satellites (Mahfouz et al., 2019) exhibited certain features of self-organization by determining and controlling their individual attitude. However, the prior studies were lacking in the interpolation quality, as only the simplest inverse-distance weights interpolator was employed.

Let us note here, that no data that has been obtained in a real space mission is used in the article. In our numerical experiments, we use geomagnetic field models to simulate the "actual" magnetic field (external for spacecraft), we use the same models with noise added to them to simulate onboard magnetometers "measurements", and we derive all the statistical properties of the geomagnetic field by analyzing the same models.

The paper has the following structure. Section one establishes the orbits of the four spacecraft that comprise the required formation. Section two introduces the Kriging interpolation algorithms and describes the construction of the necessary statistical framework (empirical semivariograms and models to fit them). Section three, describes the interpolation quality, shows how it can be improved by using the historical measurements, and provides the example of using the interpolated data in the attitude determination loop of a serviced spacecraft. Finally, the conclusion wraps up the paper by discussing the results and prospects of their application.

2. Orbital configuration

As we consider an example of ionospheric mission (such as to study ionospheric polar plasma irregularities), the formation will be deployed at a near polar circular orbit with altitude of 500 km and inclination of 87°. We shall assume that a certain reference point is traveling along this orbit, whereas the four satellites occupy specially constructed near circular relative orbits such that the four spacecraft positions are in the vertices of a non-degenerate tetrahedron.

Relative motion of two closely orbiting satellites in the central gravity field in near circular orbits is described by the Hill-Clohessy-Wiltshire equations, which are extensively used in formation flying studies (Wiltshire and Clohessy, 1960; Hill, 1878). This implies consideration of the relative spacecraft dynamics with respect to the orbital reference, whose origin moves along the circular orbit of radius r_0 and the mean motion n. In this reference frame, z-axis is aligned with the local vertical, y-axis coincides with the normal to the orbital plane, and x-axis (along track) completes the reference frame to the right-handed triad (see Fig. 1a).

The linearized equations describing spacecraft relative motion in near circular orbits are given by

$$\begin{cases} \ddot{x} + 2n\dot{z} = u_x, \\ \ddot{y} + n^2 y = u_y, \\ \ddot{z} - 2n\dot{x} - 3n^2 z = u_z, \end{cases} \tag{1}$$

where $u = \Delta f / m$, m is the mass of the spacecraft, and Δf is the linearized resultant force acting on the spacecraft, which can include a control force or any disturbing forces. In the case of free motion, i.e. if $\Delta f = 0$, Eq. (1) admit bounded periodic solutions given by

$$\begin{cases} x(t) = c_1 \cos(nt + \alpha_0) + c_3, \\ y(t) = c_2 \sin(nt + \beta_0), \\ z(t) = \frac{c_1}{2} \sin(nt + \alpha_0), \end{cases} \tag{2}$$

where the constants $c_1, c_2, c_3, \alpha_0, \beta_0$ are determined by the initial conditions.

It is discussed in Vaddi et al. (2005), Di Mauro et al. (2019), Biktimirov et al. (2020) how the periodic relative trajectories obtained from the solutions in Eq. (2) can be maintained in the presence of disturbing forces, which include any forces acting on the spacecraft apart from the central Newtonian gravity force. As our paper is not focused on the formation maintenance control algorithms, we shall model the orbital motion of the four spacecraft comprising the tetrahedron formation in the central gravity field, assuming that the disturbances are rejected according to the algorithms proposed in Di Mauro et al. (2019), Biktimirov et al. (2020). However, in spite of orbit corrections we shall introduce variations of the distances between the satellites in our formation by the special choice of initial conditions so as to see that proposed interpolation algorithms are applicable under realistic conditions when the formation maintenance is not carried out with ideal accuracy, which could ensure, for instance, a perfectly constant distance between satellites 1 and 2.

The initial conditions determining the reference trajectories are provided in Table 1. Given two options specified in Chernyshov et al. (2016) for the intersatellite distances (500 m or greater than 1 km), we chose the latter, because we aim to use interpolation algorithms that have advantage at greater distances. Hence, we chose the initial conditions such that during one orbital period the intersatellite distances vary from 2 to 5 km (as shown in the plot of Fig. 2a). This entails the value of the parameter ρ, which is an auxiliary quantity responsible for intersatellite distances (as seen from the Table 1 and Eqs. (2)), to be $\rho = 1430$ m. This value is used in all subsequent simulations. Let us note that the average edge length of the tetrahedron as it orbits the Earth equals about 3 km. This distance is further referred to as the characteristic or average intersatellite distance.

The relative trajectories are shown in Fig. 1b. Thus, two spacecraft out of the four are sent to move in almost the

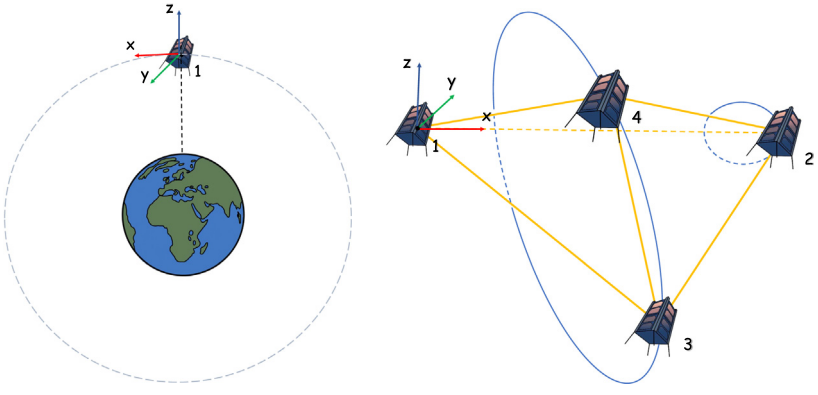

(a) Orbital reference frame (b) Relative orbits of the formation

Fig. 1. Orbital reference frame and the orbital configuration of the four-satellite formation.

Table 1
Initial conditions for the tetrahedron vertices reference trajectories.

Tetrahedron Formation Initial Conditions					
Satellite	c_1	c_2	c_3	α_0	β_0
Satellite 1	0	0	0	0	0
Satellite 2	$2\rho/5$	0	$2\rho\sqrt{5/3}$	0	0
Satellite 3	2ρ	$\rho\sqrt{5}$	$\rho\sqrt{5/3}$	$-\arctan(1/\sqrt{2})$	$\arctan(\sqrt{2})-\pi$
Satellite 4	2ρ	$\rho\sqrt{5}$	$\rho\sqrt{5/3}$	$\arctan(1/\sqrt{2})$	$-\arctan(\sqrt{2})$

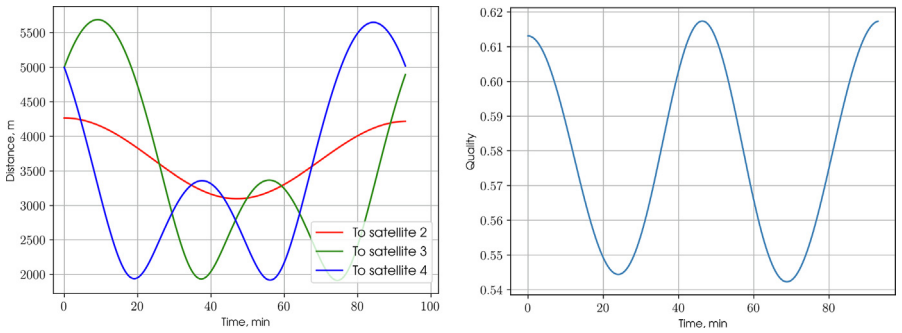

(a) Intersatellite distances (b) Tetrahedron Quality

Fig. 2. Distances between the formation satellites and the formation quality.

leader–follower formation keeping to the same circular orbit (perturbed by a non-zero value of the 2nd satellite c_1 constant), whereas the other two spacecraft are sent to a relative orbit shown in Fig. 1b (these two satellites move along the same relative orbit separated only by a phase difference). Note that as satellite 1 moves in the circular orbit and coincides with the origin of the orbital reference frame, in which all relative trajectories are described, its relative trajectory is a stationary point (the origin of the orbital reference frame), as seen from the constants given for its initial conditions in Table 1.

The measure of the resulting tetrahedron quality is introduced as (Daly, 1994; Paschmann and Daly, 1998):

$$Q = 12\frac{(3V)^{2/3}}{L}, \tag{3}$$

where V is the volume of the tetrahedron and L is the sum of squared lengths of all tetrahedron's edges. The value of Q varies from 0 for any degenerate configuration (when all four vertices belong to the same plane) to 1 for any regular tetrahedron. It is shown in Shestakov et al. (2019) that maximizing the minimum quality along the orbit in the central gravity field, one obtains $Q = 1/\sqrt[3]{5} \approx 0.585$. Let us note here that the constants in Table 1 correspond to the initial conditions derived for the maximum quality case (Shestakov et al., 2019) except c_1 for satellite 2 (non-zero value of c_1 is actually responsible for the relative orbit of the second satellite shown in Fig. 1b, which would have been a stationary point for $c_1 = 0$). The choice of non-zero c_1 value for spacecraft 2 slightly degrades the quality of tetrahedron (see Fig. 2b) as compared to the optimal case (Shestakov et al., 2019).

3. Interpolation algorithms

Kriging. Kriging algorithms (Wackernagel, 1995) are a family of Gaussian process regression methods to interpolate any quantities to be estimated at any unobserved location within a given region, for which some observations are available. Unlike inverse distance weights (IDW) interpolator and splines, which use predetermined analytical formulae defining the smoothness of the resulting curves and dependent only on the measurements obtained at a number of points in the vicinity of the interpolated location, Kriging is based on statistical models and properties of the estimated quantity such as spatial autocorrelation. Thus, Kriging not only constructs the surface of estimated values, but also provides representation of the reliability or accuracy of the obtained solution. This section briefly introduces the Kriging algorithm we shall employ for in-orbit geomagnetic field estimation in our numerical experiments.

Let us denote a vector to a point in the region of interest by $\mathbf{R}$, and the vector of the magnetic field measured at this point by $\tilde{\mathbf{B}}(\mathbf{R})$.

Similar to IDW, the estimate is computed the weighted sum of measurements in the vicinity of the interpolated point:

$$\widehat{\mathbf{B}}(\mathbf{R}_0) = \sum_{j=1}^{N} \kappa_j \tilde{\mathbf{B}}(\mathbf{R}_j) \tag{4}$$

where $\mathbf{R}_0$ is the point where interpolation is computed, $\widehat{\mathbf{B}}$ is the predicted value of the magnetic field, $\mathbf{R}_j$ are the available data points in the vicinity of $\mathbf{R}_0$, κ_j are the weights, N is the number of available data points. However, unlike

IDW, the weights κ_j are calculated to reflect the spatial correlation between $\mathbf{R}_j$ and $\mathbf{R}_0$.

The measured function $\widetilde{\mathbf{B}}(\mathbf{R})$ is assumed to be stationary, which implies the translation-invariance of the mean $\mathbf{b}$[1]

$$\forall \mathbf{R}: \quad \mathsf{E}\left[\widetilde{\mathbf{B}}(\mathbf{R})\right] = \mathbf{b} \tag{5}$$

where E is the expected value, and the covariance $C(h)$ (for Ordinary Kriging (OK) algorithm it is the scalar distance that is taken into account, other Kriging algorithms are based upon direction between points):

$$\begin{aligned} \forall \mathbf{R}_i, \mathbf{R}_j: \quad \left|\mathbf{R}_i - \mathbf{R}_j\right| &= h \\ \operatorname{cov}\left(\widetilde{\mathbf{B}}(\mathbf{R}_i), \widetilde{\mathbf{B}}(\mathbf{R}_j)\right) &= C\left(\mathbf{R}_i - \mathbf{R}_j\right) \overset{\text{OK}}{=} C(h) \end{aligned} \tag{6}$$

where $\mathbf{R}_i$ and $\mathbf{R}_j$ are radius-vectors to the data points ($i, j \in \{\overline{1, N}\}$), h is the distance between those points, which is also called lag distance, $C(h)$ is the translation-invariant function of covariance.

Variance minimization. Ordinary Kriging is known as the best linear unbiased estimator (Wackernagel, 1995). The unbiasedness is achieved by setting the 1-norm of the coefficients vector $\boldsymbol{\kappa}$ from Eq. (4) equal to 1:

$$\mathsf{E}\left[\widehat{\mathbf{B}}(\mathbf{R}_0)\right] = \mathsf{E}\left[\widetilde{\mathbf{B}}(\mathbf{R}_0)\right] = \mathbf{b} \iff \sum_{i=1}^{N} \kappa_i = 1 \tag{7}$$

Then the best estimate is guaranteed by minimizing the variance of the estimator prediction, using Eq. (7), which yields the following system of $i + 1$ equations (one equation for each respective vector $\mathbf{R}_i$, and one is the constraint imposed on $\boldsymbol{\kappa}_j$) for the weights κ_j:

$$\begin{cases} \sum_{j=1}^{N} \kappa_j \gamma\left(\mathbf{R}_i - \mathbf{R}_j\right) + \varkappa = \gamma(\mathbf{R}_i - \mathbf{R}_0), \\ \sum_{j=1}^{N} \kappa_j = 1, \end{cases} \tag{8}$$

where positions of measurement points $\mathbf{R}_i$ and $\mathbf{R}_j$ are considered to be known, $\varkappa$ is the Lagrangian multiplier of the minimization problem constraint, $\gamma(\mathbf{R}_i - \mathbf{R}_0)$ is the so-called semivariance defined as half of the variance between adjacent measurements. Semivariance and covariance (semivariances are also translation-invariant) are related as follows:

$$\begin{aligned} \gamma\left(\mathbf{R}_i - \mathbf{R}_j\right) &= \tfrac{1}{2}\mathsf{D}\left[\widetilde{\mathbf{B}}(\mathbf{R}_i) - \widetilde{\mathbf{B}}(\mathbf{R}_j)\right] = \\ &= \sigma^2 - C\left(\mathbf{R}_i - \mathbf{R}_j\right)), \end{aligned} \tag{9}$$

where D denotes variance.

The weights $\boldsymbol{\kappa}$ are obtained as a solution to the system of Eqs. (8), however, prior to solving this system, semivariances $\gamma(h)$ need to be computed. This is usually done with the use of available data sets, which are believed to reflect the statistical properties of the interpolated quantity. The steps to compute $\gamma(h)$ are (Wackernagel, 1995):

- use available data points to plot the differences in the interpolated quantity versus their lag distance h;
- construct the so-called experimental or empirical semivariogram by grouping similar lags h, lag similarity is defined in terms of lag tolerance, which is a hyperparameter of the method;
- fit the empirical semivariogram with a parametric semivariogram model function by choosing a suitable model and estimating its parameters, e.g. by a least squares fit.

A plot of semivariance is called a semivariogram.

Each point of an empirical semivariogram corresponds to all pairs of available dataset points separated by distance h, for which the sum of the squared difference between their values is computed:

$$\begin{aligned} \forall \mathbf{R}_i, \mathbf{R}_j \quad &: \quad \left|\mathbf{R}_i - \mathbf{R}_j\right| = h \\ \gamma(h) \quad &= \tfrac{1}{2N_h} \sum_{(i,j)=1}^{N_h} \left(\widetilde{\mathbf{B}}(\mathbf{R}_i) - \widetilde{\mathbf{B}}(\mathbf{R}_j)\right)^2, \end{aligned} \tag{10}$$

where N_h is the total number of the sampled points pairs.

IGRF-13 Semivariograms. Empirical semivariograms which will be subsequently employed by the interpolator are created with the use of the data obtained from IGRF-13 model. It stands to reason that it captures the necessary statistical properties of the geomagnetic field as the candidate models – proposed by various research groups for inclusion in IGRF – prior to becoming IGRF constituents are subjected to statistical tests (Thébault et al., 2015). On the other hand, IGRF has its accuracy, which is considered to be limited by a combination of two types of error, namely error of commission where there is a difference between the IGRF and the part of the field that it is attempting to model, and error of omission where the error is the part of the field that the IGRF is not attempting to model (Macmillan and Finlay, 2011). The errors of commission for the epochs for which satellite data are available are estimated to be within 5–10 nT root mean square (rms) of the true value (Macmillan and Finlay, 2011). The error of omission is dominated by the crustal field and the rms value is estimated to be 200–300 nT (Macmillan and Finlay, 2011).

If, for instance, the interpolated data are used in the loop of a satellite attitude determination system as described in Mahfouz et al. (2019), it is important to find out how much the interpolation accuracy is influenced by the semivariogram constructed from the IGRF model, if the actual field is different. In other words, the question is how do the IGRF errors influence the resulting empirical semivariogram. In order to quantify the effect, we have analyzed several empirical semivariograms and compared their effect on the Kriging weights. Fig. 3 presents semivariograms for pure IGRF-13 model, IGRF-13 model with added zero mean white noise (standard deviation 200

[1] Let us note here that this assumption can be weakened by introducing trends as it is done in the Universal Kriging (UK) algorithm. This study is conducted with the Ordinary Kriging (OK) algorithm, which does rely on the translation-invariance hypothesis.

nT), IGRF-13 model with added zero mean white noise (standard deviation 400 nT), and the direct dipole model (Ovchinnikov et al., 2018). Four data sets are obtained as the four models' outputs at locations distributed in a cube of edge-length 50 km, whose center moves along the orbit specified earlier. Each set contains 20000 samples.

As one would have expected, the greater is the noise we add, the more shapeless the point cloud becomes. The semivariograms presented in the plots of Fig. 3 do not provide a very clear indication as to the best semivariance model that fits the empirical data. However, the definition of the empirical semivariogram in Eq. (10) allows averaging the point clouds within certain intervals along the lag distance axis. The averaging reduces the number of bins, for which the semivariogram data points are obtained, and the size of these bins is determined by the lag distance tolerances. There are no general rules for determining the lag tolerances, however choosing the bin size is found to be important, and is based on the knowledge of the phenomenon under consideration (?).

Empirical semivariogram is initially constructed for all possible h-s we have in our pool of observations. Since there are thousands of possible h-s, empirical semivariogram looks like a cloud. The averaging is used to decrease the number of points and to give semivariogram a form of one-dimensional discontinuous function, which is easy to fit. All values of h are organized into equal bins, and inside those bins all values are averaged with simple arithmetic mean. An example of semivariograms obtained by such averaging is shown in the Fig. 4 where data corresponds do the pure IGRF-13 model.

Continuing the averaging procedure until the plots (see Fig. 5) retain only 10 bins, we can clearly distinguish the trend of variogram. Using this technique, we can compare the Fig. 3 plots obtained for the four different data sets. The resulting comparison is presented in Fig. 5.

The baseline semivariogram in this figure is the blue IGRF-13 with no noise added. Comparing other models with the baseline allows us to draw the following conclusions:

1. For smaller relative distances the direct dipole model is indistinguishable from IGRF-13.
2. At greater distances, however, the direct dipole model has a different slope than that of IGRF models. This affects the fitted model function parameters, and subsequently, solutions of the system of equations for weights κ_i.
3. Depending on the noise level for different IGRF models, only the value of the displacement along the ordinate axis changes. The trend is approximately the same.

Taking into account the fact that semivariograms are used as weights of linear system of Eqs. (8), the displacement along the ordinate axis becomes insignificant for the solution, since it does not change the solution of this system (i.e. weights κ_i). The slope, which becomes different for the direct dipole model at greater distances, is a more important parameter in this case. Since it is mostly the ordinate axis displacement that changes with the noise level, it can be inferred that even very noisy geomagnetic field data can still be used within the Kriging approach.

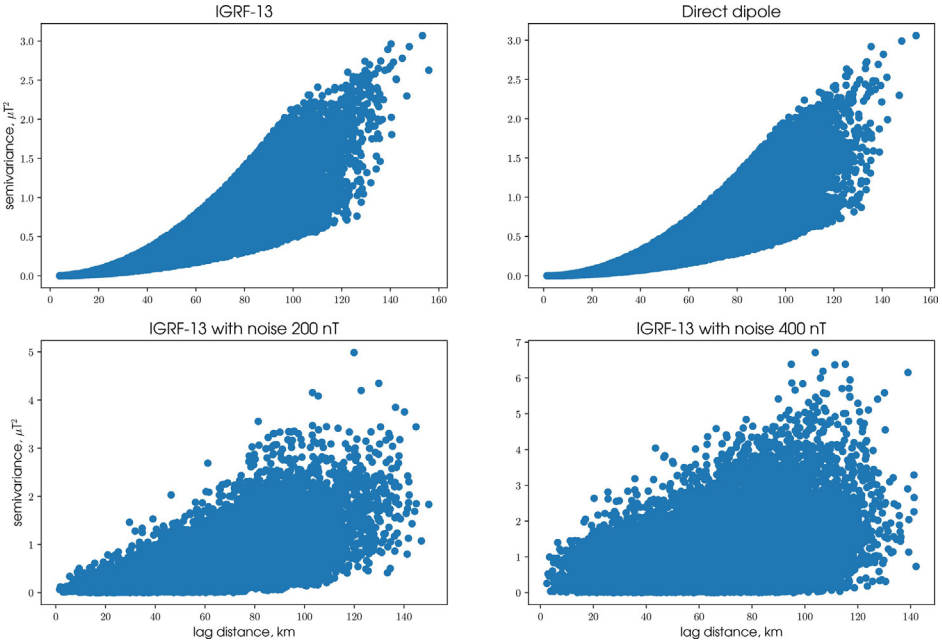

Fig. 3. Empirical semivariograms for different magnetic field models.

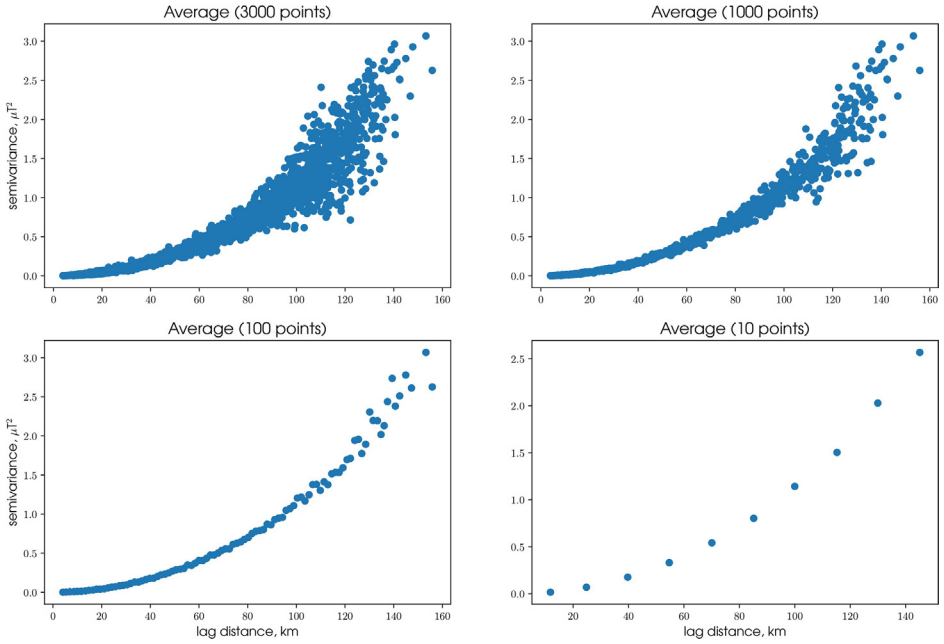

Fig. 4. Averaging of empirical semivariogram for IGRF-13 without noise.

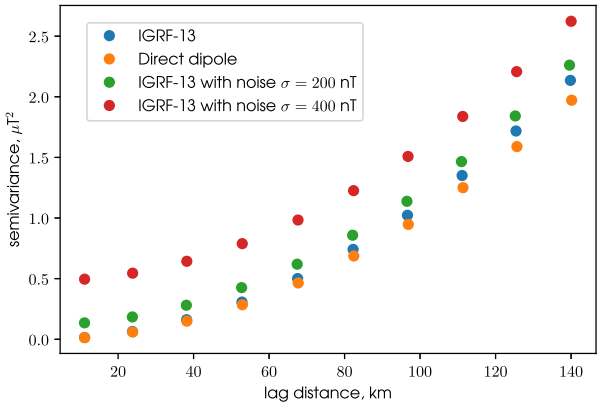

Fig. 5. Comparison of empirical semivariogram trends for different field models.

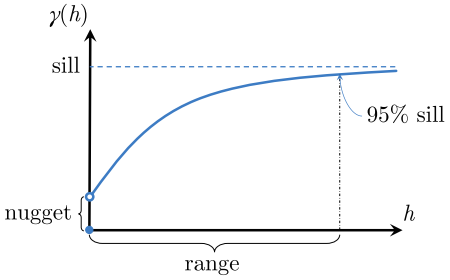

Fig. 6. Semivariogram model function parameters.

After we have collected enough data for empirical semivariogram, we can approximate it with analytical models (e.g. linear, spherical, Cauchy, powered exponential, etc. (Wackernagel, 1995)). This step is necessary because of discontinuity in the Eq. (10).

As illustrated in Fig. 6 the model functions are usually characterized by the following parameters:

- nugget – discontinuity level at the origin,
- sill – $\lim_{h\to\infty}\gamma(h)$,
- range – distance h, at which $\gamma(h) = 0.95$ sill.

There is a large variety of such models, but as in the Figs. 3–5, the function should possess the inflection point (the point where the 2nd derivative changes sign) – this feature is found in the powered exponential and Matern functions. Extensive numerical experiments with the latter, however, invariably resulted in its lower accuracy (in terms of root-mean-square error RMSE) with respect to the former. For this reason, we shall only consider the powered exponential model given by:

$$\gamma(h) = \begin{cases} c_0 + c\left(1 - \exp\left[-\left(\frac{h}{a}\right)^{v}\right]\right) & , \quad h > 0 \\ 0 & , \quad h = 0 \end{cases} \tag{11}$$

where c_0 is the nugget, $c_0 + c$ is the sill, a is a distance parameter, defined as approximately one third of a range of the semivariogram, and v is the power of the exponent. If $v = 1$ the model is called exponential, and if $v = 2$ it is called Gaussian.

Fig. 7(a), (b) and (c) present the results of fitting powered exponential model to the empirical semivariograms, which are based on the IGRF-13 model without any noise, with 200 nT noise, and with 400 nT noise, respectively. The parameters from Eq. (11) are presented in Table 2.

As can be seen from Table 2, all parameters except c_0 are nearly the same, which is consistent with the earlier discussion on the ordinate displacements for these semivariograms.

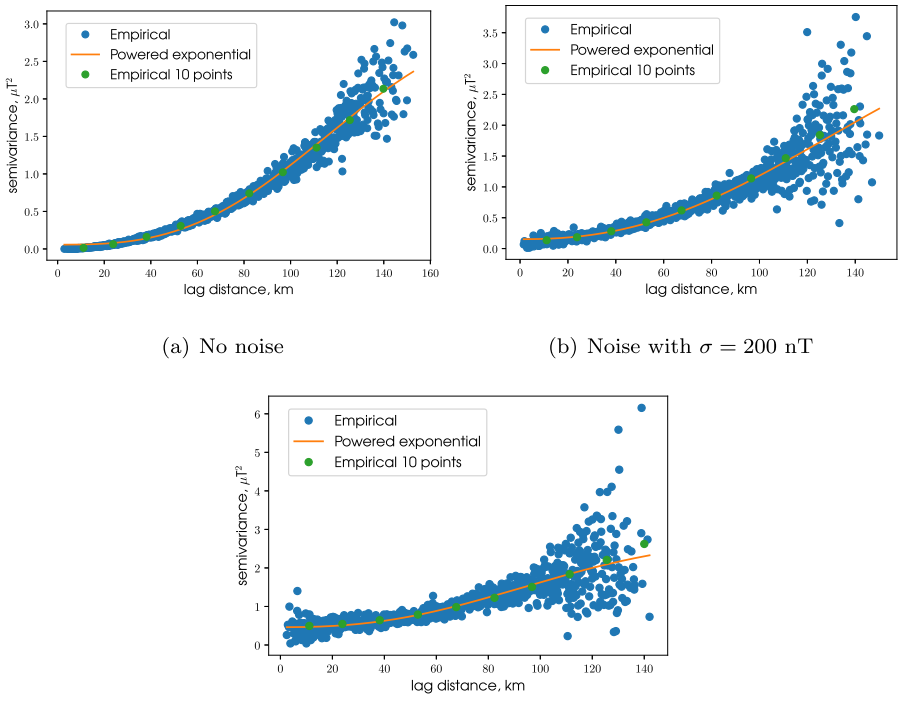

(a) No noise

(b) Noise with $\sigma = 200$ nT

(c) Noise with $\sigma = 400$ nT

Fig. 7. Fitting of the powered exponential function into empirical semivariograms, based on IGRF-13 models with different level of noise.

Concluding this Section, we shall note again that adding noise to the geomagnetic field model does not significantly change the Kriging solution, and therefore in all subsequent simulations we shall use the powered exponential model fit obtained for the IGRF-13 model without the noise component (first raw in Table 2). Thus, weights $\boldsymbol{\kappa}$, acquired from any noise-level IGRF model (up to 400 nT), can be used for the interpolation, which takes as observations actual magnetic field measurements.

4. Simulation results

All simulation in this Section are conducted with the following parameters:

- The orbits for the four formation satellites are described in Section 2 with specified relative motion in form of Table 1 ($\rho = 1430$ m). Spacecraft do not have attitude errors.
- The model of the Earth magnetic field is IGRF-13. The value of the magnetic field in current location of each satellite is measured by the magnetometer with error, modeled as Gaussian noise with $\sigma_{\text{mm}} = 10$ nT and zero mean.
- The interpolation algorithm is Ordinary Kriging (see Eq. (8)) with powered exponential model. The data is taken and processed in the orbital frame of the 1st satellite (see Fig. 1).

Experiment 1 – single-point measurements vs interpolation. The graphs of Fig. 8 present the comparison of the geomagnetic field interpolated measurements with a single satellite measurements data. The interpolation is made for the location of satellite 1 along its orbit. The plot depicts the errors of direct measurement of the geomagnetic field (black dots) and the errors of the interpolation results (colored dots). The plots are made for just one run (one orbit) and for the location of just one satellite, however the errors are qualitatively representative of what we obtained in multiple numeric experiments.

Fig. 8 contains 4 subfigures, presenting the comparison for the three components of the magnetic field vector and for its absolute values, respectively. The graphs of Fig. 8 clearly show that the characteristic error of satellite mea-

Table 2
Function parameters for different magnetic field models.

Standard deviation of model noise, [nT]	c_0, $[\mu T^2]$	c, $[\mu T^2]$	a, [km]	v
0	0.04	2.48	364	2.77
200	0.15	2.86	390	2.52
400	0.5	2.13	335	2.73

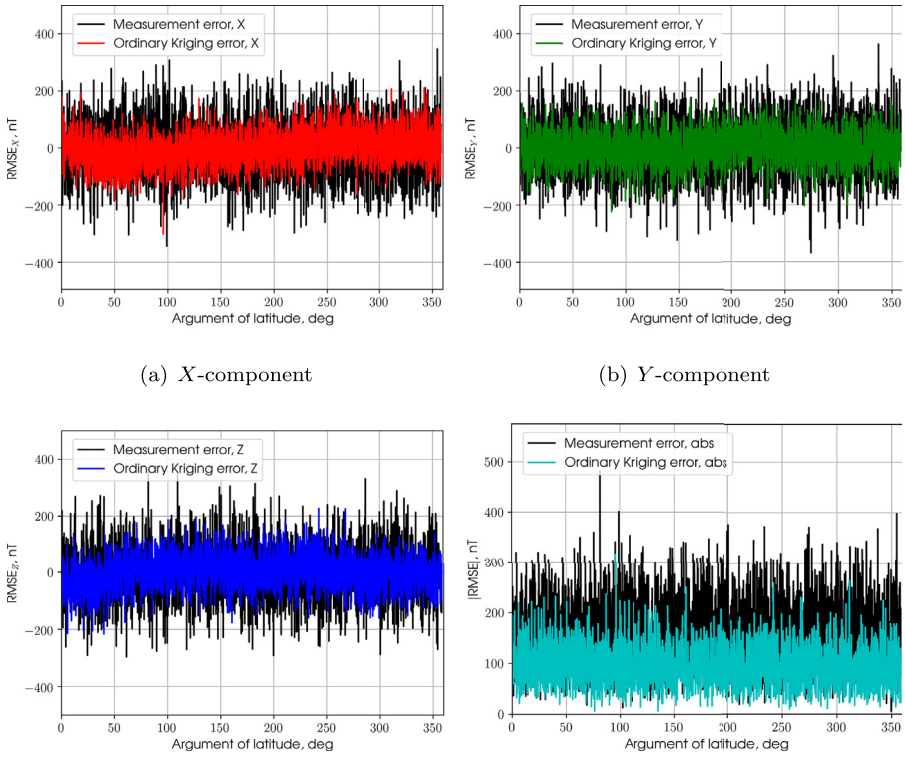

(a) X-component (b) Y-component

(c) Z-component (d) Absolute value

Fig. 8. The error of magnetic field interpolation by Ordinary Kriging in comparison with measurements error of Satellite #1 versus argument of latitude θ on the orbit.

surements with interpolation in a formation is visibly smaller than that for the conventional single-point measurements. The latter, which will be further referred to as *singleton measurements* implies that a satellite does not use observations of other spacecraft (i.e. does not use interpolation).

Experiment 2 – formation size. Comparing different semivariograms in terms of mean-squared errors, we argued in Section 3 that even the noise of 400 nT will not significantly affect the interpolation result. This experiment is to check this assumption. Fig. 9, shows how average RMSE (for the interpolated absolute value of the geomagnetic field at the locations of all the four satellites along their orbits) is dependant on the characteristic size of this formation. The average is computed from 100 runs of one orbital period and different noise seeds.

The dotted horizontal line in the figure is the RMSE δ for measurements carried out by each satellite in singleton mode without interpolation. The interpolation is considered to be "successful" if the corresponding RMSE level is below this line. There are also 3 graphs, which show the error level of measurements with Kriging interpolation for the semivariograms, based on models of magnetic fields with different levels of noise: 0, 200 and 400 nT – red, green and blue, respectively. The plot shows that interpolation graphs start to diverge only after the intersatellite distance reaches 12.5 km. It indicates that all semivariogram models

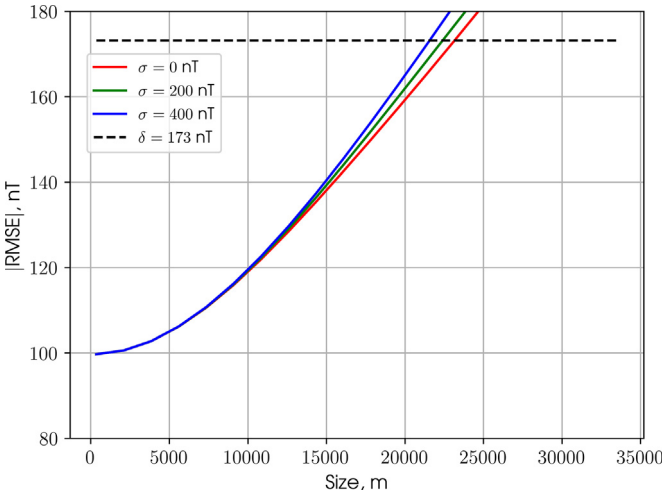

Fig. 9. RMSE of the magnetic field interpolation versus characteristic size of the formation.

are equally applicable for formation size less than 12 km. Using the size of formation of 7 km, which mostly covers all previously discussed ionospheric missions, the Kriging interpolation can double the measurement accuracy.

Using measurements history. The usage of measurements history implies adding prior measurements carried out by the formation spacecraft for the current interpolation. The prior measurements are made in the previous locations

of the spacecraft along their respective orbits and we have to assume that the measured field does not change during the time that passed since the measurements were made. This, and also the formation size considerations given in the previous experiment limit the history of measurements to those made no earlier than 0.2 s prior to the current time, which corresponds to the distance of approximately 1.5 km back along the orbit. The time period of 0.2 s between measurements is considered only in the areas of the quasi-homogeneous fields, whereas the usage of history measurements with this period in the area of quick and strong field variations, such as magnetotails, will lead to the loss of interpolation accuracy.

The result of increasing the number of data points in the interpolator is shown in Fig. 10. The graphs of Fig. 10 are analogous to those presented in Fig. 8, and show the result of the magnetic field measurements' accuracy enhancement in terms of RMSE. The accuracy enhancement in each component for the interpolated data with history points is noticeably greater than in Fig. 8, where no measurements history is used.

Table 3 presents the quantitative comparison of the history experiment results. It compares the mean μ_{abs} and standard deviation σ_{abs} for RMSE shown in Fig. 10(d), and also standard deviations estimated for plots Fig. 10 (abc) (σ_X, σ_Y, σ_Z). The conclusion about accuracy enhancement is also confirmed by Fig. 11 (analogous to Fig. 9), where the RMSEs of the magnetic field interpolation and measurement is compared with singleton measurements, all dependent on the formation size.

The most important observation from Fig. 11 is that even for formations of large size the RMSEs of satellites measurements with interpolation is always way under the line of direct field measurement δ (without interpolation). Comparing it with Fig. 9, the size 7.5 km corresponds to the accuracy improvement by 4 times (2 times without history). This implies that the quality of interpolation is highly dependant on the number of measurement points. And increasing this number in any way, such as using history measurements, generally leads to a better accuracy of the method.

Attitude determination. In our previous experiments we have ascertained that the proposed interpolation technique does allow obtaining better data for the external magnetic field than that measured by each satellite individually. We shall now show an example of how this can be employed in the attitude determination loop of a satellite, which does not belong to the modeled formation, but receives the interpolated data as a service. To make this example simple, we shall not describe here the Extended Kalman filter, which it is customary to use in the attitude determination loop, but instead will show the advantages of using the interpolated data through a simple deterministic TRIAD algorithm (Markley and Crassidis, 2014).

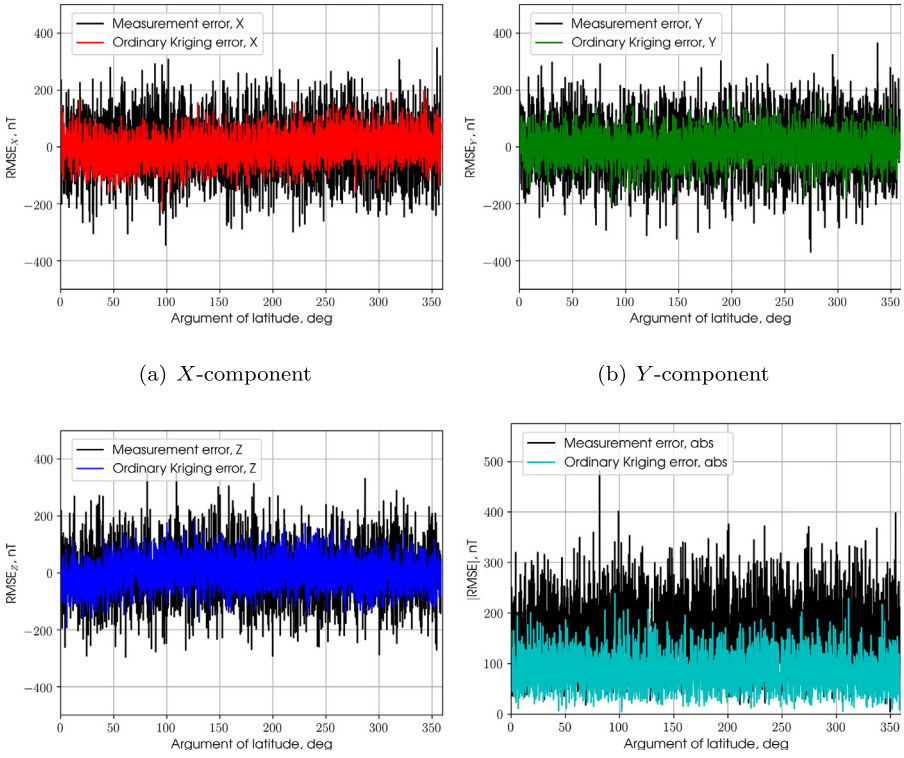

(a) X-component (b) Y-component

(c) Z-component (d) Absolute value

Fig. 10. The error of magnetic field interpolation by Ordinary Kriging in comparison with measurements error of Satellite #1 versus argument of latitude θ on the orbit, using the history of previous measurements.

Table 3
Comparison of means and estimated standard deviations of the RMSEs from Fig. 10 (interpolation with history measurements) and Fig. 8 (interpolation without history measurements).

Interpolation type	μ_{abs}, [nT]	σ_{abs}, [nT]	σ_X, [nT]	σ_Y, [nT]	σ_Z, [nT]
With history	84.4	91.6	53.2	51.2	54.1
Without history	95.9	104.3	60.9	57.7	62.1

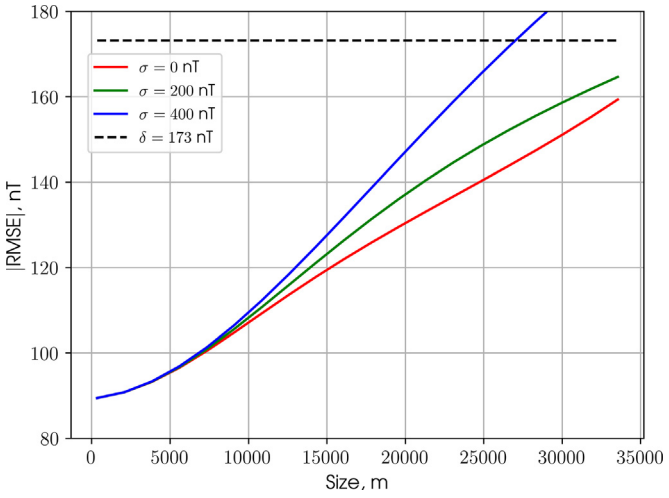

Fig. 11. RMSE of the magnetic field interpolation versus characteristic size of the formation, using the history of previous measurements.

TRIAD is the procedure to obtain the satellite's attitude parameters (in the form of the direction cosine matrix (DCM)) given two pairs of vectors represented in two different reference frames. One pair is, for instance, the direction to the Sun and the local geomagnetic field vector represented in the inertial frame (usually calculated via onboard models). We shall use those vectors representations in the orbital frame, which can be transformed to the inertial frame and back. The second pair consists of the same vectors, but measured by the sensors and, consequently represented in the satellite body-frame.

For this experiment we shall simulate rotational dynamics of a spacecraft located in the service zone of the formation and compare the results of its attitude determination for TRIAD using onboard model for geomagnetic field or the interpolated multipoint measurements. The truncated onboard models (especially in CubeSats, where computational power is scarce) usually differ from complete IGRF models by a value of ±100 nT. Beside that, they are not able to predict such events as magnetic storms, which can change the external magnetic field around the spacecraft up to 500 nT (Lakhina et al., 2004). In this regard the interpolated geomagnetic field vector (given in inertial or orbital reference frame) appears to be advantageous. It should be noted, however, that the main problem of magnetometer-based attitude determination lies not in the shortcomings of the model, but rather in difficulty of identifying the magnetometer bias due to residual magnetisation of the satellite itself. However, this problem is beyond the scope of this article.

We shall compare, how the interpolation of the magnetic field model affects the resulting DCM. To this end we are going to obtain two DCMs, one of which is built upon onboard-model value of the magnetic field $\mathbf{B}^{\text{orb}}_{\text{model}}$, and the other one is built upon interpolated value $\widehat{\mathbf{B}}^{\text{orb}}_{\text{int}}$. Interpolated estimate is based on the actual values of the Earth magnetic field $\mathbf{B}^{\text{orb}}_{\text{actual}}$, which is obviously different from the truncated board model. We consider this difference to be $\sigma_{\text{model}} = 500$ nT, and model the dependency between those fields as Gaussian noise with mentioned standard deviation and zero bias:

$$\mathbf{B}^{\text{orb}}_{\text{actual}} = \mathbf{B}^{\text{orb}}_{\text{model}} + \mathcal{N}\left(\mathbf{0}, \sigma^2_{\text{model}}\mathbf{I}\right) \tag{12}$$

Measurements $\widetilde{\mathbf{B}}^{\text{body}}_{\text{meas}}$ are acquired with magnetometers, which usually have observation errors. We shall model magnetometer measurements with unbiased Gaussian noise, whose standard deviation is $\sigma_{\text{mm}} = 10$ nT, to minimize the effect of observation noise on the DCM reconstruction:

$$\widetilde{\mathbf{B}}^{\text{body}}_{\text{meas}} = \mathbf{A}^{\text{orb}\to\text{body}}\mathbf{B}^{\text{orb}}_{\text{actual}} + \mathcal{N}\left(\mathbf{0}, \sigma^2_{\text{mm}}\mathbf{I}\right) \tag{13}$$

where $\mathbf{A}^{\text{orb}\to\text{body}}$ is true DCM, which converts vectors' representations from the orbital reference frame to the body-frame.

Another pair of vectors, which is used for TRIAD algorithm, consists of the Sun direction $\mathbf{S}^{\text{orb}}_{\text{model}}$ obtained from an onboard model and sun sensor output $\widetilde{\mathbf{S}}^{\text{body}}_{\text{meas}}$. The Sun direction model outputs an inertial frame representation, which depends only on the Julian date chosen in the following simulation to be 2458940.19. The vector then is converted to the orbital frame (zero RAAN and known inclination 87°) and taken as the model value $\mathbf{S}^{\text{orb}}_{\text{model}}$. The sun sensor measurements are modeled equivalently with magnetic field measurements from Eqs. (12) and (13), but normalised and with standard deviations $\sigma_{\text{sunmodel}} = 10^{-9}$ and $\sigma_{\text{sunsensor}} = 10^{-4}$.

Thus, having two pairs of vectors $\mathbf{B}$ and $\mathbf{S}$, we can define the TRIAD-algorithm in our case. Estimates of the matrix $\mathbf{A}^{\text{orb}\to\text{body}}$ are following:

$$\begin{aligned}
&\mathbf{t}^{\text{b}}_1 = \widetilde{\mathbf{S}}^{\text{body}}_{\text{meas}} \quad && \mathbf{t}^{\text{b}}_2 = \mathbf{t}^{\text{b}}_1 \times \frac{\widetilde{\mathbf{B}}^{\text{body}}_{\text{meas}}}{\left\|\widetilde{\mathbf{B}}^{\text{body}}_{\text{meas}}\right\|} && \mathbf{t}^{\text{b}}_3 = \mathbf{t}^{\text{b}}_1 \times \mathbf{t}^{\text{b}}_2 \\
&\mathbf{t}^{\text{o}}_1 = \mathbf{S}^{\text{orb}}_{\text{model}} && \mathbf{t}^{\text{o}}_2 = \mathbf{t}^{\text{o}}_1 \times \frac{\mathbf{B}^{\text{orb}}}{\left\|\mathbf{B}^{\text{orb}}\right\|} && \mathbf{t}^{\text{o}}_3 = \mathbf{t}^{\text{o}}_1 \times \mathbf{t}^{\text{o}}_2 \\
&\widehat{\mathbf{A}}^{\text{orb}\to\text{body}} && = \left[\mathbf{t}^{\text{b}}_1|\mathbf{t}^{\text{b}}_2|\mathbf{t}^{\text{b}}_3\right]\left[\mathbf{t}^{\text{o}}_1|\mathbf{t}^{\text{o}}_2|\mathbf{t}^{\text{o}}_3\right]^{\top}
\end{aligned} \tag{14}$$

Substituting $\mathbf{B}^{\text{orb}}$ from Eq. (14) either with $\mathbf{B}^{\text{orb}}_{\text{model}}$ or with $\widehat{\mathbf{B}}^{\text{orb}}_{\text{int}}$, we will get matrices $\widehat{\mathbf{A}}^{\text{orb}\to\text{body}}_{\text{model}}$ and $\widehat{\mathbf{A}}^{\text{orb}\to\text{body}}_{\text{int}}$ respectively, which should be compared with each other.

DCMs are computed for the orbit, defined in Section 2, and converted into the Euler angles – roll, pitch, yaw; and into the axis-angle representation. Simulation results are presented in Fig. 12. The peaks in the first four plots of Fig. 12 are explained by a known weakness in the TRIAD algorithm which becomes sensitive to errors when the angle between the Sun direction and the geomagnetic field direction is small. Such is the case when the argument of latitude approaches the value of 60°.

The kinematics for spacecraft relative motion and rotational dynamics are simulated via following equations:

$$\begin{aligned} \dot{\mathbf{A}} \quad &= \mathbf{A}\left[\boldsymbol{\omega}^{\text{body}} - \mathbf{A}^{\top}\mathbf{n}^{\text{orb}}\right]_{\times}, \\ \mathbf{J}\dot{\boldsymbol{\omega}}^{\text{body}} \quad &+\boldsymbol{\omega}^{\text{body}} \times \mathbf{J}\boldsymbol{\omega}^{\text{body}} = \mathbf{T}^{\text{body}}_{\text{grav}} + \mathbf{T}^{\text{body}}_{\text{dist}}, \end{aligned} \tag{15}$$

where $\mathbf{A} = \mathbf{A}^{\text{body}\to\text{orb}}$ and $\mathbf{A}^{\top} = \mathbf{A}^{\text{orb}\to\text{body}}$ are DCMs which relate orbital and body reference frames, $\boldsymbol{\omega}^{\text{body}}$ is spacecraft's absolute angular velocity in the body frame, $\mathbf{n}^{\text{orb}} = (0 \quad n \quad 0)^{\top}$ is the mean-motion vector in the orbital frame, $[\mathbf{x}]_{\times}$ is the skew-symmetric matrix, which represents cross-product operator for vector $\mathbf{x}$, such that $[\mathbf{x}]_{\times}\mathbf{y} = \mathbf{x} \times \mathbf{y}, \forall \mathbf{x}, \mathbf{y} \in \mathbb{R}^3$, $\mathbf{J}$ is an inertia tensor in principal (body) axes with components $(11, 14, 9)\text{g} \cdot \text{m}^2$, $\mathbf{T}^{\text{body}}_{\text{grav}}$ and $\mathbf{T}^{\text{body}}_{\text{dist}}$ are gravitational and disturbance torques expressed in the body frame. The disturbance torque is modeled as

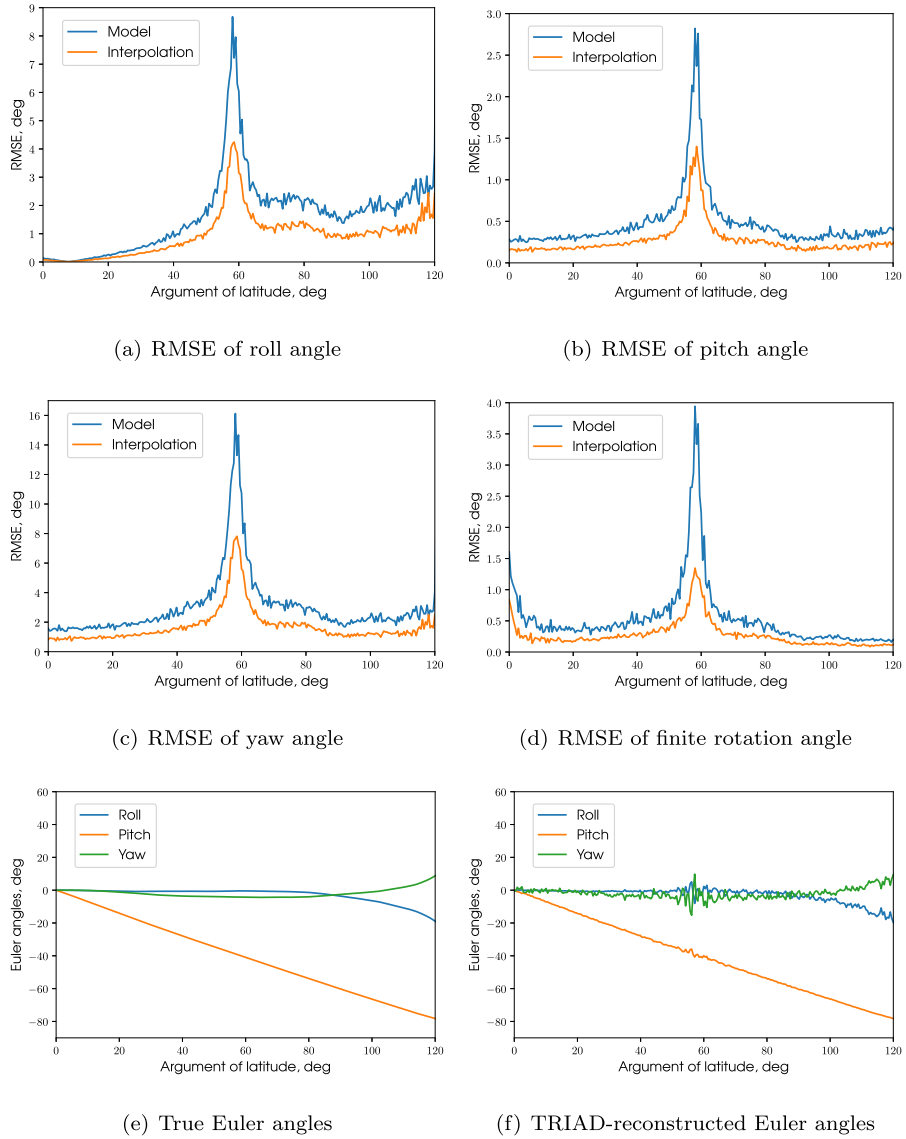

(a) RMSE of roll angle

(b) RMSE of pitch angle

(c) RMSE of yaw angle

(d) RMSE of finite rotation angle

(e) True Euler angles

(f) TRIAD-reconstructed Euler angles

Fig. 12. The error of Euler angles and quaternion angle determination of Satellite #1, using the TRIAD algorithm, versus argument of latitude θ on the orbit. Subfigures (a)–(d) show the RMSEs of aforementioned angles, reconstructed with TRIAD algorithms, based on the model values (blue) and interpolated values (orange) of the Earth magnetic field. Subfigures (e)–(f) show the example of Euler angles evolution on the orbit for Satellite #1 and how they are reconstructed with TRIAD, based on interpolated magnetic field values. (For interpretation of the references to colour in this figure legend, the reader is referred to the web version of this article.)

the unbiased Gaussian noise with standard deviation $\sigma_{\text{torque}} = 10^{-7}\text{N} \cdot \text{m}$. Simulations are held with initial conditions: $\mathbf{A} = \mathbf{A}^{\top} = \mathbf{I}_{3\times 3}, \boldsymbol{\omega}^{\text{body}} = \mathbf{0}_3$, where $\mathbf{I}$ is an identity matrix. Satellite rotational dynamics as described by the Euler angles is shown in Fig. 12(e).

The results of RMSE calculation as shown in Fig. 12 indicate that the interpolation of geomagnetic field enhances the accuracy of the satellite attitude determination even with simple TRIAD up to 3° in the case of strong divergence of the onboard model with the actual magnetic field. These results can be improved, using the Extended Kalman Filter or other specific algorithm of the attitude determination (and control) system.

To sum up the results of the experiments above, it can be said that they provide conclusive evidence to acknowledge the positive outcomes of the feasibility study we carried out. However, it must be further investigated, whether the proposed concept will turn out applicable in an actual space mission with actual measurements. On one hand, it may seem that multipoint measurements are always better than single point measurements, because they allow averaging out errors and rejecting obvious outliers. On the other hand, collecting such measurements comes at a price of establishing intersatellite communication with its latency, extra power consumption, need to synchronize formation spacecraft clocks and a common reference frame with respect to which the data exchange is conducted.

We have reasons to believe, that the concept itself of using Kriging family of interpolators to process multipoint measurements of natural phenomena will remain valid if implemented in a real mission as long as there are means of constructing empirical semivariograms. For instance, the example we used with the geomagnetic field measurements is based on the IGRF models which are proven to bear statistical resemblance with the actual field. This lets us claim that the geomagnetic experiment can be reproduced in reality. The method we demonstrated here is based on certain assumptions, which may not hold true in reality (such as Gaussian noise as a difference of the actual field from the IGRF model), but this difficulty can be solved by using other Kriging interpolators which can be applicable under various conditions (e.g. Kriging with trends or spatio-temporal Kriging). This can be made a subject of a future study.

Further concept validation, could be carried out with the use of the measurement data from relevant real formation missions, however the available data sets are obtained for formations (MMS, THEMIS) that operated at distances, which are significantly greater than those, at which our method is expected to be advantageous (formation size less than 10 km). However, we plan to conduct the real-data experiment as Skoltech university is preparing a swarm mission comprising four magnetically controlled CubeSats as an intersatellite communication technology demonstration. We hope that the coordinated data exchange will become a part of the mission program and this will allow us demonstrating a proof of concept in orbit.

5. Conclusion

This paper considers an extra function, a satellite formation can carry out, namely, data exchange and interpolation. We studied a mission, whose orbital configuration is similar to tentative ionospheric mission for multipoint spatial plasma measurements in a polar orbit. As an example of the multipoint measurements geomagnetic field was considered.

We showed that even for a four-satellite formation, multipoint measurements and appropriate interpolation methods can produce comparatively precise instantaneous maps of the measured quantity. For the geomagnetic field we outlined the procedure of how the Kriging interpolation can be carried out, studied different variogram models and chose the best fitting one. We also established the size of the 3D local map that can be constructed with the four available satellites and discussed how the quality of this map can be improved by using measurements history.

We concluded the paper by quantifying how the enhanced geomagnetic field data can be used to improve the attitude determination routine quality for any satellite, which happens to be within the coverage of the servicing formation. It appears that even for such simplistic attitude determination routine as TRIAD the result can be improved by 1–3 degrees, which is quite significant for university ionospheric missions, that rely on the low-cost COTS and require pointing accuracy of a few degrees.

On completing this study, we believe that the Kriging interpolation algorithms (of which there is more than a mere Ordinary Kriging we used in this paper) is worthy of close attention of the researchers involved with multipoint space measurements. One other thing, that we should like to point out is that with the advent of megaconstellations, when networking satellites will occupy large regions of space, such service as we showed through the example of four-satellite formation, may actually become as universal as that of GNSS.

Declaration of Competing Interest

The authors declare that they have no known competing financial interests or personal relationships that could have appeared to influence the work reported in this paper.

Acknowledgment

This work is funded by RFBR, project number 19–38-90278.

References

Afanasev, A., Ivanov, A., Mahfouz, A., Pritykin, D., 2020. Attitude control algorithms in a swarm of cubesats: Kriging interpolation and coordinated data exchange. Adv. Astronaut. Sci. 173, 3–22.

Biktimirov, S., Ivanov, D., Sadretdinov, T., Omran, B., Pritykin, D., 2020. A multi-satellite mission to illuminate the earth: Formation control based on impulsive maneuvers. Adv. Astronaut. Sci. 173, 463–474.

Bonin, G.R., Roth, N., Armitage, S., Newman, J., Risi, B., Zee, R., 2015. Canx4 and canx5 precision formation flight: Mission accomplished!.

Chernyshov, A., Chugunin, D., Mogilevsky, M., et al., 2016. Approaches to studying the multiscale ionospheric structure using nanosatellites. Geomag. Aeron. 56, 72–79.

Chernyshov, A., Chugunin, D., Mogilevsky, M., Petrukovich, A., 2020. Studies of the ionosphere using radiophysical methods on ultra-small spacecrafts. Acta Astronaut. 167, 455–459.

Daly, P.W., 1994. The tetrahedron quality factors of csds. Technical report MPAe–W–100–94–27. Max Planck Inst. fur Aeronomie Tech. Rep.Katlenburg-Lindau, Germany.

Di Mauro, G., Spiller, D., Bevilacqua, R., D'Amico, S., 2019. Spacecraft formation flying reconfiguration with extended and impulsive maneuvers. J. Franklin Inst. 356, 3474–3507.

Fish, C., Swenson, C., Crowley, G., et al., 2014. Design, development, implementation, and on-orbit performance of the dynamic ionosphere cubesat experiment mission. Space Sci. Rev. 181, 61–120.

Friis-Christensen, E., Lühr, H., Hulot, G., 2006. Swarm: A constellation to study the earth's magnetic field. Earth, Planets Space 58, 351–358.

Grasso, M., Renga, A., Fasano, G., et al., 2020. Design of an end-to-end demonstration mission of a formation-flying synthetic aperture radar (ff-sar) based on microsatellites. Adv. Space Res.

Guzman, J.J., Edery, A., 2004. Mission design for the mms tetrahedron formation. In: 2004 IEEE Aerospace Conference Proceedings (IEEE Cat. No.04TH8720), vol. 1, p. 540.

Hill, G.W., 1878. Researches in the lunar theory. Am. J. Math. 1, 5–26.

Krieger, G., Moreira, A., Fiedler, H., Hajnsek, I., Werner, M., Younis, M., Zink, M., 2007. Tandem-x: A satellite formation for high-resolution sar interferometry. IEEE Trans. Geosci. Remote Sens. 45, 3317–3340.

Lakhina, G., Alex, S., Tsurutani, B., Gonzalez, W., 2004. Research on historical records of geomagnetic storms.

Loizzo, R., Guarini, R., Longo, F., Scopa, T., Formaro, R., Facchinetti, C., Varacalli, G., 2018. Prisma: The italian hyperspectral mission, in. In: IGARSS 2018–2018 IEEE International Geoscience and Remote Sensing Symposium, pp. 175–178.

Macmillan, S., Finlay, C., 2011. The International Geomagnetic Reference Field. Springer, Netherlands, Dordrecht, pp. 265–276.

Mahfouz, A., Pritykin, D., Afanasev, A., Annenkova, A., Latyshev, K., 2019. Coordinated attitude determination and control in a swarm of cubesats.

Markley, F.L., Crassidis, J.L., 2014. Fundamentals of spacecraft attitude determination and control, vol. 33. Springer.

Nicholas, A.C., Attrill, G.D.R., Dymond, K.F., Budzien, S.A., Stephan, A.W., Fritz, B.A., Routledge, G.J., Miah, J.A., Brown, C.M., Marquis, P.J., Finne, T.T., Mitchell, C.N., Watson, R.J., Kataria, D.O., Williams, J., 2019. Coordinated Ionospheric Reconstruction CubeSat Experiment (CIRCE) mission overview. In: Pagano, T.S., Norton, C.D., Babu, S.R. (Eds.), CubeSats and SmallSats for Remote Sensing III. International Society for Optics and Photonics, SPIE, pp. 105–117.

Ovchinnikov, M., Penkov, V., Roldugin, D., Pichuzhkina, A., 2018. Geomagnetic field models for satellite angular motion studies. Acta Astronaut. 144, 171–180.

Paschmann, G., Daly, P.W., 1998. Analysis Methods for Multi-Spacecraft Data. ISSI Scientific Reports Series SR-001, ESA/ISSI, vol. 1. ISBN 1608-280X, 1998. ISSI Scientific Reports Series 1.

Roscoe, C.W.T., Vadali, S.R., Alfriend, K.T., Desai, U.P., 2011. Optimal formation design for magnetospheric multiscale mission using differential orbital elements. J. Guid. Control Dyn. 34, 1070–1080.

Sadeghi, S., Emami, M., 2017. Multi-spacecraft studies of the auroral acceleration region: From cluster to nanosatellites. Adv. Space Res. 59, 1173–1188.

Shestakov, S., Ovchinnikov, M., Mashtakov, Y., 2019. Analytical approach to construction of tetrahedral satellite formation. J. Guid. Control Dyn. 42, 2600–2614.

Stephens, G.L., Vane, D.G., Boain, R.J., Mace, G.G., Sassen, K., Wang, Z., Illingworth, A.J., O'connor, E.J., Rossow, W.B., Durden, S.L., Miller, S.D., Austin, R.T., Benedetti, A., Mitrescu, C., the CloudSat Science Team, 2002. THE CLOUDSAT MISSION AND THE A-TRAIN: a new dimension of space-based observations of clouds and precipitation. Bull. Am. Meteorol. Soc. 83, 1771–1790.

Thébault, E., Finlay, C., Alken, P., Beggan, C., Canet, E., Chulliat, A., Langlais, B., Lesur, V., Lowes, F., Manoj, C., Rother, M., Schachtschneider, R., 2015. Evaluation of candidate geomagnetic field models for igrf-12. Earth Planets Space 67.

Vaddi, S., Alfriend, K.T., Vadali, S., Sengupta, P., 2005. Formation establishment and reconfiguration using impulsive control. J. Guid. Control Dyn. 28, 262–268.

Wackernagel, H., 1995. Multivariate Geostatistics. Springer, Berlin, Heidelberg.

Wiltshire, R., Clohessy, W., 1960. Terminal guidance system for satellite rendezvous. J. Aerosp. Sci. 27, 653–658.